Fragmentation paths in dynamical models

M. Colonna,[1] A. Ono,[2] and J. Rizzo[1]
[1]*Laboratori Nazionali del Sud–Istituto Nazionale Fisica Nucleare, I-95123 Catania, Italy*
[2]*Department of Physics, Tohoku University, Sendai 980-8578, Japan*
(Received 28 April 2010; revised manuscript received 5 October 2010; published 18 November 2010)

We undertake a quantitative comparison of multifragmentation reactions, as modeled by two different approaches: the antisymmetrized molecular dynamics (AMD) and the momentum-dependent stochastic mean-field (SMF) model. Fragment observables and pre-equilibrium (nucleon and light cluster) emission are analyzed, in connection with the underlying compression-expansion dynamics in each model. Considering reactions between neutron-rich systems, observables related to the isotopic properties of emitted particles and fragments are also discussed, as a function of the parametrization employed for the isovector part of the nuclear interaction. We find that the reaction path, particularly the mechanism of fragmentation, is different in the two models and reflects on some properties of the reaction products, including their isospin content. This should be taken into account in the study of the density dependence of the symmetry energy from such collisions.

DOI: 10.1103/PhysRevC.82.054613 PACS number(s): 25.70.Pq, 24.10.Lx, 24.10.Pa

I. INTRODUCTION

Because of the analogies between the nuclear forces and the Van-der-Waals interaction, the nuclear matter equation of state (EOS) foresees the possible occurrence of phase transitions from the liquid to the vapor phases [1,2]. Already in the 1980s, these phenomena were linked to the experimentally observed multifragmentation mechanism (i.e., the sudden breakup of an excited nuclear system into many pieces [3,4]). However, in the search for signatures of a phase transition, one has to consider that nuclei are finite systems. New features may appear in addition to standard thermodynamics. Moreover, the nuclear phase diagram is explored with the help of nuclear reactions, where out-of-equilibrium effects may also be present. These considerations have led, on one hand, to significant developments of the thermodynamics of finite systems and to new definitions of the phase transition, following the concepts of statistical physics [5,6]. On the other hand, many efforts have been devoted to the study of the reaction dynamics and to the characterization of the fragmentation mechanism, also in connection with the possible appearance of the signals expected for a phase transition at thermodynamical equilibrium [7–13].

It is generally believed that, in a heavy-ion collision at Fermi energies, because of the initial compression and/or thermal excitation, the composite nuclear system may expand and reach density and temperature values inside the coexistence region of the nuclear matter phase diagram [2,9,14]. In violent collisions, multifragment configurations are characterized by a large degree of chaoticity and a huge amount of the available phase space is populated. Finally, several features observed in the exit channel can be related to the thermodynamical (equilibrium) properties of phase transitions in finite systems, independently of the specific mechanism that has driven the whole process [12,13]. However, there remain some aspects that reflect the nature of the reaction dynamics and of the fragmentation path, mostly related to out-of-equilibrium effects. Indeed the interplay between the compression-expansion dynamics and the onset (and nature) of clusterization affects significantly the fragment kinematical properties and the appearance of collective flow effects. A thorough study of this dynamics also allows one to access information on the nuclear matter compressibility. Moreover, the specific features of the fragmenting source, such as its mass, charge, and excitation energy, are also strongly depending on the pre-equilibrium dynamics and on the time instant where clusterization sets in.

Hence, a quantitative understanding of multifragmentation data requires a careful investigation of the whole dynamical path. Because of the complexity of the nuclear many-body problem, two main lines of approximation have been followed so far. On one hand, the class of molecular dynamics (MD) approaches employ, to represent a many-body state, a product of single-particle states, with or without antisymmetrization, where only the mean positions and momenta are time dependent [15–20]. In almost all these approaches, the width is fixed and is the same for all wave packets. The use of localized wave packets induces many-body correlations (analogous to those in classical dynamics) in the particle propagation in the nuclear field, as well as in hard two-body scattering that is treated stochastically. On the other hand, mean-field approaches (and stochastic extensions) follow the time evolution of the one-body distribution function (the semiclassical analog of the Wigner transform of the one-body density matrix), according to approximate equations where higher order correlations are neglected (mean-field approximation), apart from the correlations introduced by the residual two-body collisions. In the stochastic extension of the model, a fluctuation source term is added to the average collision integral, to account for the stochastic nature of two-body scattering [2,21–23].

A comparison of the predictions given by models of the two classes, concerning multifragmentation scenarios at Fermi energies (30–50 MeV/nucleon), was recently undertaken [24]. The models considered are: the stochastic mean-field (SMF) model including momentum dependence [25] and the antisymmetrized molecular dynamics (AMD) model [14]. It was observed that, although in the SMF case fragment emission is more likely connected to the spinodal decomposition mechanism (i.e., to mean-field instabilities), in the AMD

approach many-body correlations have a stronger impact on the fragmentation dynamics, leading to the earlier development of density and momentum fluctuations.

In the present article we will discuss quantitatively the impact of the different approximations employed in the two models on several particle and fragment observables of experimental interest. This also allows one to establish to which extent some of the observed features may be considered more robust or general (i.e., not much depending on the details of the fragmentation path) and of the models under consideration. By studying reactions with neutron-rich systems, we also investigate isospin observables, in connection with the density dependence of the symmetry energy and the underlying reaction dynamics.

II. DESCRIPTION OF THE MODELS

A. Basic framework

In both SMF and AMD approaches, the time evolution of the system is described in terms of the one-body distribution function f (or a Slater determinant), as ruled by the nuclear mean-field (plus Coulomb interaction for protons) and the residual interaction (i.e., hard two-body scattering). The equation can be represented in the form of the so-called Boltzmann-Langevin equation [21,22],

$$\frac{\partial f}{\partial t} = \{H[f], f\} + I[f] + \delta I[f], \tag{1}$$

where the coordinates of spin, isospin, and phase space are not shown for brevity. $H[f]$ is the self-consistent one-body Hamiltonian, $I[f]$ is the average two-body collision integral, and $\delta I[f]$ stands for the stochastic source term [21,22].

The effect of the stochastic term $\delta I[f]$ is considered for the value of the distribution function f_α in each phase space cell α. For example, one may decompose the phase space into square cells of the volume $(2\pi\hbar)^3$. In the case of local equilibrium, the source term $\delta I[f]$ induces the fluctuation of f_α, the variance of which is given by $\langle \Delta f_\alpha^2 \rangle = f_\alpha(1 - f_\alpha)$. The correlations between different cells are usually assumed to be small, but minimal correlations are introduced for the conservation laws. In the approximate treatment of SMF presented in [26,27], the fluctuations are projected and implemented only onto the ordinary space, agitating the spatial density profile from time to time during the reaction after the local thermal equilibrium is reached.

It should be noted that the variance $\langle \Delta f_\alpha^2 \rangle = f_\alpha(1 - f_\alpha)$ with the average value f_α is achieved by choosing $f_\alpha + \Delta f_\alpha = 1$ and 0 with the probabilities f_α and $1 - f_\alpha$, respectively. Namely the fluctuation will choose A fully occupied phase-space cells, with A being the number of nucleons in the system, while the remaining part of phase space becomes empty. AMD represents this situation by using Gaussian wave packets $\propto e^{-2\nu(\mathbf{r}-\mathbf{R}_i)^2-(\mathbf{p}-\mathbf{P}_i)^2/2\hbar^2\nu}$ $(i = 1, \ldots, A)$. Each wave packet has the minimum uncertainty $\Delta x \Delta p = \frac{1}{2}\hbar$ and therefore can be regarded as a phase space cell. The width parameter $\nu = (2.5\ \mathrm{fm})^{-2}$ defines the shape of the cell in phase space.

In AMD, the right-hand side of Eq. (1) is usually decomposed in a different way for the convenience of writing a stochastic equation for the wave-packet centroids. The mean-field effect is decomposed to the motion of the centroids and the change of the shape of the one-body distributions: $\{H, f\} = \{H, f\}_{\mathrm{cent}} + \{H, f\}_{\mathrm{shape}}$. The first term $\{H, f\}_{\mathrm{cent}}$ is calculated by employing the fully antisymmetrized wave function [17], whereas $\{H, f\}_{\mathrm{shape}}$ is approximately calculated by using a test particle method [28,29]. The stochastic source term is also separated as $\delta I = \delta I_{\mathrm{coll}} + \delta I_{\mathrm{split}}$. The part δI_{coll} is the stochastic effect included in the stochastic collisions $(I + \delta I_{\mathrm{coll}})$ that move the centroids of the wave packets by choosing the scattering angle randomly. When a nucleon collides with another, $\delta I_{\mathrm{split}}$ randomly selects a Gaussian wave packet from the single-particle state that was changing its shape according to $\{H, f\}_{\mathrm{shape}}$, by splitting it into possibilities of Gaussian wave packets (quantum branching or decoherence) [28,29].

Thus the main difference between the two models lies in the implementation of the stochastic term [i.e., whether the fluctuation in the momentum space is integrated out (in SMF) or not (in AMD)]. Moreover, in AMD, when a collision happens, two entire nucleons are moved to new wave packets in phase space, whereas it is not necessarily the case in SMF. Therefore, the fluctuation is expected to have a stronger impact on the collision dynamics in AMD than in SMF.

B. Effective interaction

The isospin- and momentum-dependent effective interaction employed in the SMF model is derived via an asymmetric extension of the GBD force [30,31], leading to the BGBD potential [25,32,33]. In the AMD model, we employ the Gogny interaction which is composed of finite-range two-body terms and a zero-range density-dependent term.

The corresponding nuclear matter EOS can be written as $(E/A)(\rho, \beta) = (E/A)(\rho) + E_{\mathrm{sym}}(\rho)\beta^2 + O(\beta^4) + \cdots$, where the variable $\beta = (\rho_n - \rho_p)/\rho$ defines the isospin content, being ρ_τ $(\tau = n, p)$ the neutron or proton density and ρ the total density. We use a soft equation of state for symmetric nuclear matter [compressibility modulus $K_{\mathrm{NM}}(\rho_0) = 215$ MeV for BGBD and $K_{\mathrm{NM}} = 228$ MeV for the Gogny force]. In Fig. 1 we report the EOS, as a function of the density ρ, for symmetric nuclear matter, $\beta = 0$, at zero temperature. We can easily adjust the parameters of the interaction to change the density dependence of symmetry energy (E_{sym}) without changing the EOS of symmetric nuclear matter. The density behavior of the symmetry energy, $E_{\mathrm{sym}}(\rho)$, is shown in Fig. 2. We remind one that this quantity gets a kinetic contribution directly from basic Pauli correlations and a potential part from the highly controversial isospin dependence of the effective interactions [34,35]. For the BGBD force, we adopt two different parametrizations of the symmetry energy: "asy-soft," that gives a flat behavior around normal density, followed by a decreasing trend at large density, and "asy-stiff," where the symmetry energy exhibits an almost linear increase with density [36]. The Gogny (D1) force [37] has a quite similar $E_{\mathrm{sym}}(\rho)$ to the "asy-soft" parametrization of BGBD, whereas another parametrization [38] of the Gogny force has $E_{\mathrm{sym}}(\rho)$ similar to the "asy-stiff" version of BGBD. Hence, in

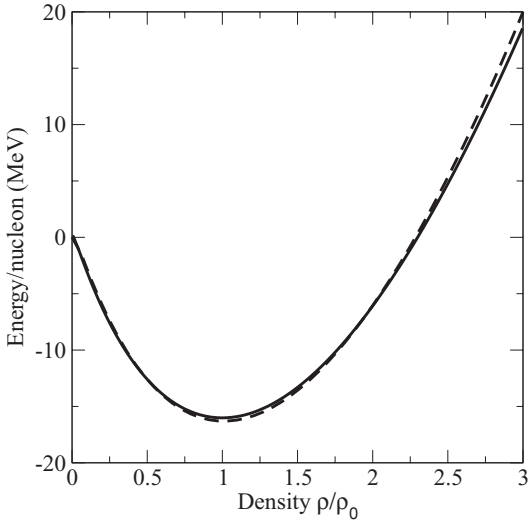

FIG. 1. Equation of state (EOS) of symmetric nuclear matter, corresponding to the Gogny (solid) and BGBD (dashed) interactions.

the following we will use the labels "asy-soft" and "asy-stiff" for the Gogny forces as well.

Within the considered form of the nuclear interaction, the isovector terms depend explicitly on the nucleon momentum $k = p/\hbar$, leading to the splitting of neutron and proton effective masses. The mean-field potential felt by neutrons and protons in asymmetric nuclear matter ($\beta = 0.2$) is presented in Fig. 3, as a function of the momentum k, for three density values and for the adopted interactions (asy-soft and asy-stiff). As an effect of the momentum dependence, the difference between neutron and proton potentials decreases with k, becoming negative at high momenta, especially in the asy-soft case. This corresponds to the proton effective mass being smaller than the neutron one in neutron-rich matter. Moreover, one can see that the difference between neutron and proton potentials is larger, at low density, in the asy-soft case, corresponding to the larger value of the symmetry energy (see Fig. 2), whereas the opposite holds above normal density. The results of the BGBD and Gogny forces look very close to each other below and around the Fermi momentum, for both neutrons and protons. However, from the different shape of the momentum dependence in the BGBD interaction, with respect to the Gogny force, at high momenta ($k \geqslant 3\ \mathrm{fm}^{-1}$) potential are less attractive in the BGBD case. This discrepancy should not affect our comparison because we are interested in reactions at Fermi energies.

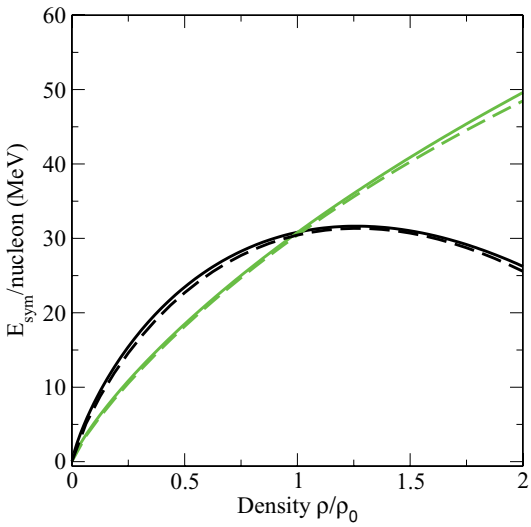

FIG. 2. (Color online) Parametrizations of the density behavior of the symmetry energy adopted in the calculations: asy-soft (black lines), asy-stiff (gray lines). Solid lines correspond to the Gogny forces, whereas dashed lines are for the BGBD forces.

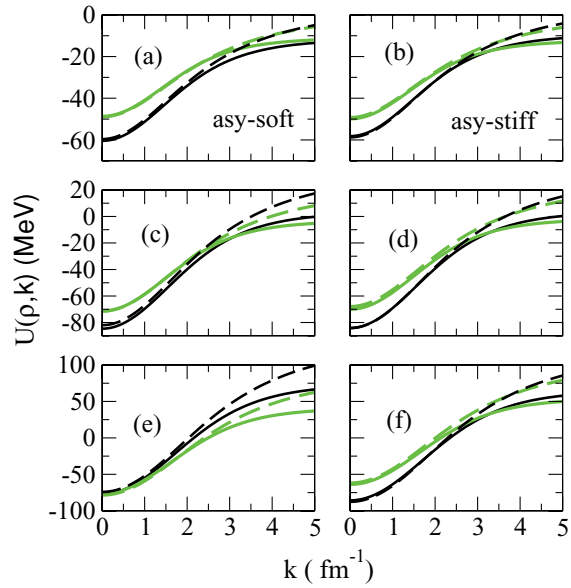

FIG. 3. (Color online) Mean-field potential, for neutrons (gray lines) and protons (black lines) in asymmetric matter ($\beta = 0.2$) at density $\rho = 0.085\ \mathrm{fm}^{-3}$ [(a) and (b)], $\rho = 0.17\ \mathrm{fm}^{-3}$ [(c) and (d)], $\rho = 0.34\ \mathrm{fm}^{-3}$ [(e) and (f)], as a function of the momentum k. Solid lines correspond to the Gogny forces, whereas dashed lines are for the BGBD forces. Left panels, asy-soft interaction; right panels, asy-stiff interaction.

C. Two-nucleon collision cross sections

As the two-nucleon collision cross sections ($\sigma_{pp} = \sigma_{nn}$ and σ_{pn}), we use the energy- and angle-dependent values in the free space with the maximum cutoff of 150 mb in both SMF and AMD calculations. We have confirmed that the degree of stopping reached in the reaction is similar for both calculations [24]. However, it should be noticed that these cross sections are larger than those adopted by the AMD calculation in Ref. [28].

D. Fragment identification

In the SMF model, the reaction products are reconstructed by applying a coalescence procedure to the one-body density $\rho(\mathbf{r})$ [i.e., connecting neighboring cells with density $\rho \geqslant \frac{1}{6}\rho_0$ ("liquid" phase)]. In this way one can also identify a "gas" phase ($\rho < \frac{1}{6}\rho_0$), associated with particles that leave rapidly the system (pre-equilibrium emission) and/or are evaporated. Once fragments are identified, from the knowledge of the

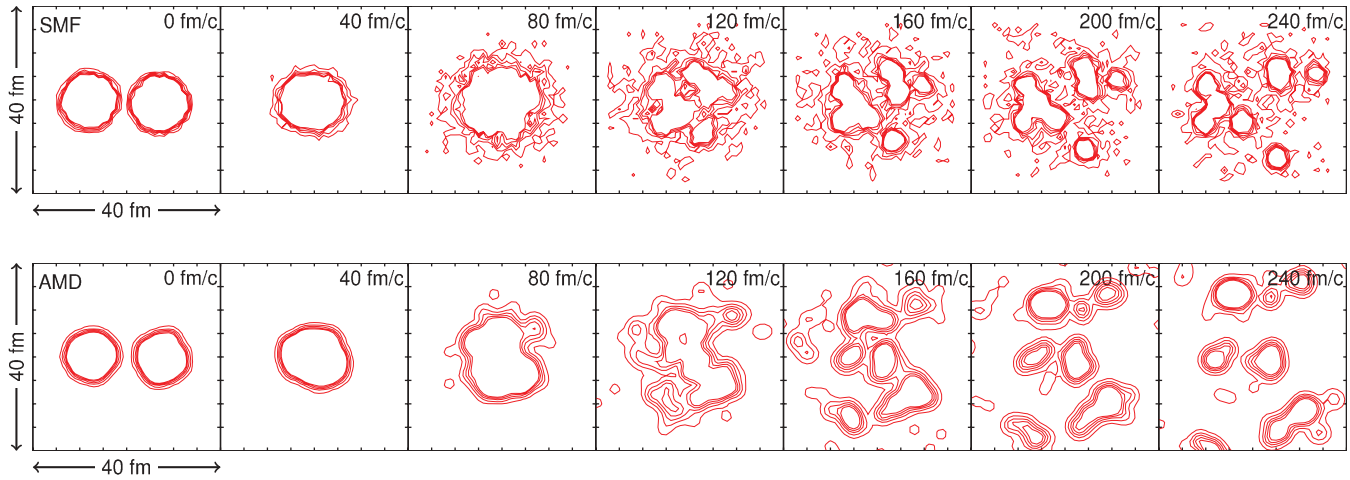

FIG. 4. (Color online) Contour plots of the density projected on the reaction plane calculated with SMF (top) and AMD (bottom) for the central reaction ^{112}Sn + ^{112}Sn at 50 MeV/nucleon, at several times (fm/c). The lines are drawn at projected densities beginning at 0.07 fm^{-2} and increasing by 0.1 fm^{-2}. The size of each box is 40 fm.

one-body distribution function, it is possible to calculate their mass, charge, and kinematical properties. This provides reasonable results for the description of the ground state of medium-heavy nuclei and for excited primary fragment properties. Fragment excitation energies are calculated by subtracting the Fermi motion, evaluated in the local density approximation, from the fragment kinetic energy (taken in the fragment reference frame) [2,26].

In the AMD model, for the state at a given time of the reaction, fragments are recognized by connecting two wave packets if the spatial distance between their centroids is less than $d_{\rm cl}$. When fragments are recognized at a late time, such as $t = 200$ fm/c, we take $d_{\rm cl} = 5$ fm, although the result does not depend on the choice except for extreme choices. When fragments are recognized at early times to characterize the dynamical evolution of the reaction, different choices of $d_{\rm cl}$ define different observables. We take a relatively small value of $d_{\rm cl} = 3$ fm in Figs. 6, 7, 12, and 13, which allows an earlier recognition of particle emissions.

Alternatively, we can employ the same fragment recognition method that is applied to the SMF calculation by applying a coalescence procedure to the density distribution $\rho(\mathbf{r})$ calculated for the AMD wave function. We have confirmed that the result well agrees with the usual method with $d_{\rm cl} = 5$ fm for fragment charge distributions (i.e., for the separation of fragments), whereas the choice of $d_{\rm cl} = 3$ fm better agrees with the coalescence procedure for the light particle emissions (i.e., for the separation of "liquid" and "gas") at early times.

III. RESULTS

We discuss some features of the fragmentation path followed in violent collisions at Fermi energies, as predicted by the SMF and the AMD models. To investigate isospin effects and the sensitivity of the results to the parametrization adopted for the symmetry energy, we will simulate central collisions of a neutron-poor and a neutron-rich system: ^{112}Sn + ^{112}Sn and ^{124}Sn + ^{124}Sn, at 50 MeV/nucleon. Within our study of fragmentation reactions, we expect to test the low-density behavior of the symmetry energy. As we will see in the following, the isospin degree of freedom can also be used as a good tracer of the reaction dynamics. An ensemble of about 100 trajectories was collected for both model calculations. The impact parameter was set equal to 0.5 fm and the initial distance between the two nuclei (at the time $t = 0$) is 15 fm. Density contour plots in the reaction plane, as obtained in the two models for one event of the ^{112}Sn + ^{112}Sn reaction, are shown in Fig. 4 at several time steps. As one can see from the figure, for this kind of reactions, both models predict that the system is initially compressed. Then expansion follows and multifragment breakup is observed. One can also observe that the expansion is faster in AMD and that the amount of emitted nucleons (the "gas" phase) is larger in SMF.

A. Compression-expansion dynamics

In this section we summarize the main findings of Ref. [24], concerning the trajectory followed by the system in the early stage of the dynamics, until fragmentation is observed. The reaction path can be characterized with the help of one-body observables, such as the radial density profile and the radial collective momentum. The radial density at a given distance r is obtained by averaging the local density $\rho(\mathbf{r})$ over the surface of a sphere of radius r. The radial collective momentum is the projection of the collective momentum at the position $\mathbf{r}$ along the radial direction, averaged over the surface of the sphere of radius r. These quantities are further averaged over the ensemble events.

In the SMF calculations [see Fig. 5(a)] the behavior of the radial density profile indicates that, after an initial compression ($t = 40$ fm/c), the system expands and finally it gets somewhat dilute, because of the occurrence of a monopole expansion, generated by the initial compression. The matter appears mostly concentrated within a given interval of the radial distance (see, for instance, the results at $t = 100$ fm/c), indicating the formation of bubblelike configurations (see also

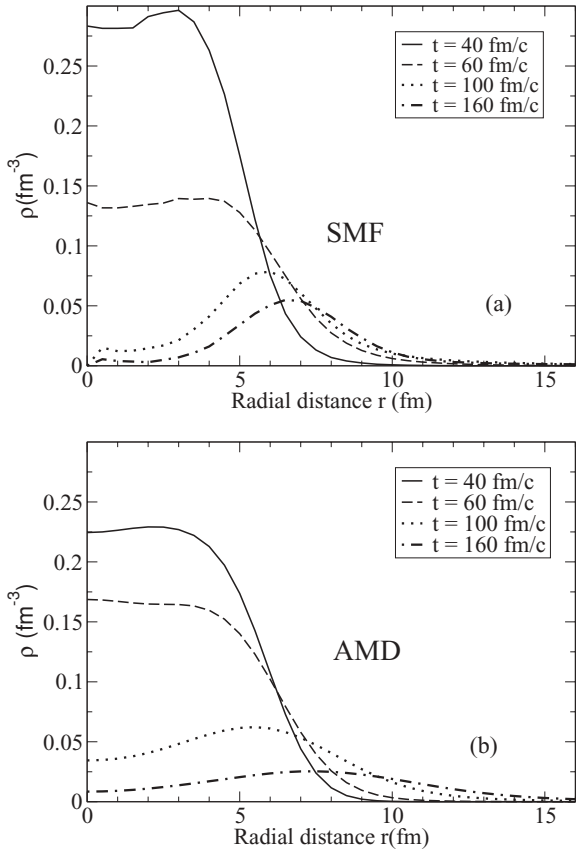

FIG. 5. Density profiles, at several times, as obtained in the SMF (a) and AMD (b) case, for the reaction ^{112}Sn + ^{112}Sn.

Fig. 4), where fragments will appear, and the central region of the system is rapidly depleted.

In AMD calculations, the density profile in Fig. 5(b) shows the time evolution of the compression and expansion, which is qualitatively similar to the SMF case. However, we notice that AMD shows broader average density distribution than SMF as the system expands, pointing to a faster expansion in the AMD, as indicated qualitatively by Fig. 4. This is confirmed also by the behavior of the collective momentum. An shown in Ref. [24], in the SMF case, after the development of an almost self-similar radial flow, the collective momentum decreases again at the surface of the system, indicating the occurrence of a counter-streaming flow, from the surface toward the interior, trying to recompact the system [39]. Correspondingly, a bump is obtained in the radial density distribution [see Fig. 5(a) at $t = 100$ fm/c]. However, the collective momentum at the surface of the expanding system keeps almost unchanged in the AMD calculations [24]. The absence of deceleration effects may indicate that the system ceases to behave as homogeneous while it expands, corresponding to the situation, of somewhat low average density, in which fragments have already appeared and are distributed widely in space. This scenario is supported by the analysis of the density fluctuation variance, that reveals an earlier growth of density fluctuations (leading to an earlier appearance of clusters) in the AMD case [24]. This can be interpreted as the reason for the faster expansion in AMD as observed in Fig. 4 at later times. We notice that early fragment formation is observed also in other N-body treatments, belonging to the class of molecular dynamics models, as shown by the quasiclassical calculations performed in Ref. [40].

In conclusion, although in the SMF case the system spends more time, as a nearly homogeneous source, at low density, and fragments are formed most likely through the spinodal mechanism [2], in the AMD case clustering effects may be present at an earlier stage. This also influences significantly the amount of particles emitted prior to fragment formation (pre-equilibrim emission), as discussed in the following.

B. Time evolution of nucleon and cluster emission

During the first stage of the reaction, hard two-body scattering plays an essential role and pre-equilibrium emission is observed (i.e., nucleons and light particles are promptly emitted from the system). This stage influences significantly the following evolution of the collision. In fact, the amount of particles and energy removed from the system affects the properties of the composite source that eventually breaks up into pieces. Hence, when discussing multifragmentation mechanisms, a detailed analysis of this early emission is in order. Figures 6 and 7 show the time evolution of the total number of neutrons and protons contained in emitted nucleons and light particles, with mass number $A \leqslant 4$, as obtained in the two models, with the two asy-EOS considered, and for the two reactions. It should be noticed that this ensemble is mainly composed of unbound nucleons in the SMF case. As shown in these figures, these particles leave the system mostly in the time interval between ≈70 fm/c and ≈120 fm/c. At later times the emission rate is reduced (see the change of slope in the lines of Figs. 6 and 7. As already pointed out in Ref. [24], a striking difference between the two models

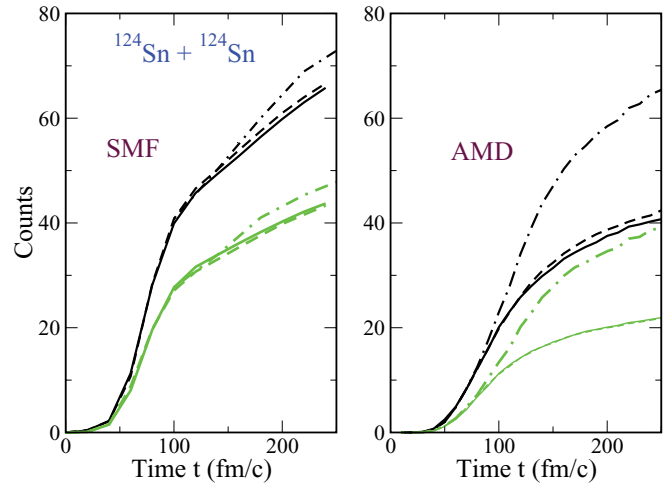

FIG. 6. (Color online) Time evolution of the total number of neutrons (black lines) and protons (gray lines) contained in emitted particles with $1 \leqslant A \leqslant 4$, in the case of the reaction ^{124}Sn + ^{124}Sn. Dashed line, asy-soft parametrization; solid line, asy-stiff parametrization. The dot-dashed lines represent the time evolution of the total number of neutrons and protons contained in emitted particles with $1 \leqslant A \leqslant 15$, for the asy-soft parametrization. Left panel, SMF results; right panel, AMD results.

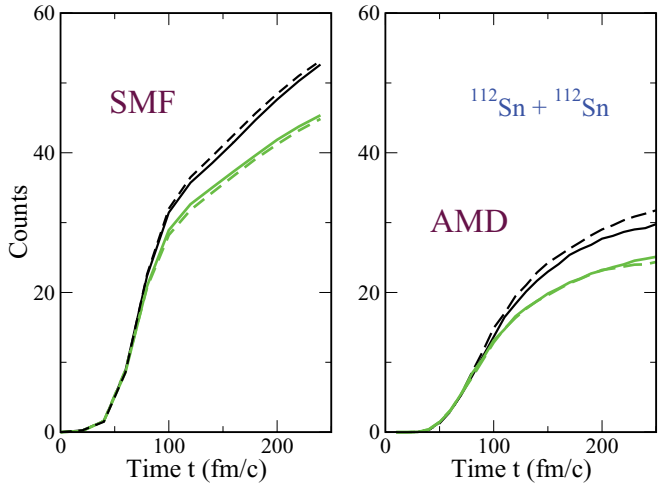

FIG. 7. (Color online) The same as in Fig. 6, for the system ^{112}Sn + ^{112}Sn.

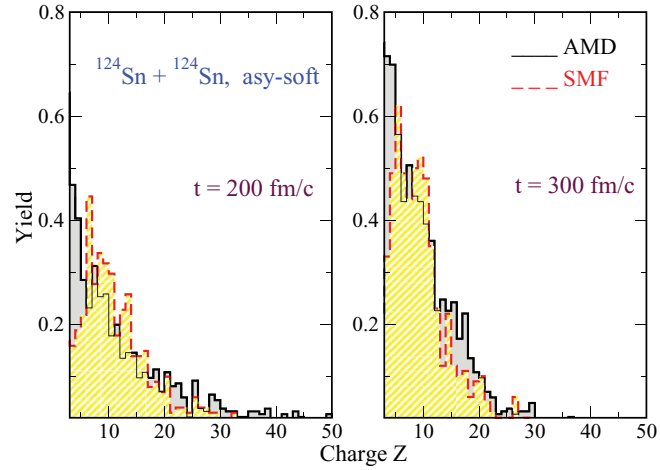

FIG. 8. (Color online) Charge distribution as obtained in AMD (solid histogram) and in SMF (dashed histogram), for the reaction ^{124}Sn + ^{124}Sn, at $t = 200$ fm/c (left) and $t = 300$ fm/c (right).

concerns the amount of particles emitted, that is larger in the SMF case. However, the average kinetic energy of this emission is similar, being 20.72 MeV/nucleon in SMF and 21.95 MeV/nucleon in AMD. The difference observed in the two models could be connected to the fact that clustering effects and many-body correlations are more efficient in AMD, because of the nucleon localization, reducing the amount of mass that goes into free nucleons and very light clusters. This effect is also connected to the different compression-expansion dynamics in the two models, as discussed in the previous section.

On the other hand, light IMFs, with mass number $5 \leqslant A \leqslant 15$, are more abundant in AMD. This is observed in Fig. 6, where the total amount of neutrons and protons contained in emitted particles with $A \leqslant 15$ is also displayed as a function of time, in the case of the asy-soft interaction (see the dot-dashed lines). In the AMD case, the emission of light IMFs starts already at around 70 fm/c and, at the time $t = 250$ fm/c, it represents a noticeable fraction of the particles emitted in the considered mass range ($A \leqslant 15$); see the difference between dot-dashed and dashed lines. Hence fragments are formed on shorter time scales in AMD, on about equal footing as light-particle pre-equilibrium emission, whereas in SMF this light IMF emission sets in at later times and is much reduced. However, one can see that the total amount of emitted nucleons belonging to particles with $A \leqslant 15$ (including free nucleons) is close in the two models (compare the dot-dashed lines at the final time in the left and right panels of Fig. 6). Hence one expects to see a similar production of IMFs with charge $A > 15$, as will be discussed in the following.

As general features, when comparing the two reactions (Figs. 6 and 7), it is seen that neutron (proton) emission is more abundant in the neutron-rich (poor) systems. Moreover, Figs. 6 and 7 also show that a larger (smaller) number of neutrons (protons) is emitted in the asy-soft case, as compared with the asy-stiff case, corresponding to a larger repulsion of the symmetry potential for the soft parametrization. This can be taken as an indication of the fact that pre-equilibrium particles are mostly emitted from regions that are below normal density (i.e., after $t \approx 70$ fm/c, during the expansion phase), where the symmetry energy is higher in the soft case (see Fig. 2).

C. Fragment properties

Now we move to discuss and compare the properties of primary fragments, as obtained in the two models. In Fig. 8 we present the charge distribution of primary IMFs ($Z > 2$) at two time instants: $t = 200$ and 300 fm/c.

Some of the fragments identified by the clustering procedure at $t = 200$ fm/c have exotic (elongated) shapes and they break up into pieces at later times. This effect is present in both models and explains the difference observed between the charge distributions calculated at $t = 200$ and $t = 300$ fm/c. In the SMF case the maximum yield corresponds to fragments having charge around $Z = 10$, as expected within a fragmentation scenario associated with spinodal decomposition [2]. The fragmentation mechanism may also be connected to the small yield of the light IMFs that, as also discussed in Sec. III B, is lower in SMF, compared to AMD. Hence the total mass that belongs to the "liquid" phase (IMFs) is reduced in SMF. This is the counterpart of the more abundant pre-equilibrium emission. The production of sizable clusters ($Z > 6$) looks closer in the two calculations. This is true especially at $t = 300$ fm/c, where the tail at large Z, which is observed at $t = 200$ fm/c and is more pronounced in AMD calculations, disappears. However, the emission of fragments with charge around 10 is slightly larger in SMF, whereas bigger fragments (with charge around 15–20) are more abundant in AMD. It should be noticed that these differences may be smoothened by the secondary decay process; see the results of Ref. [41] for SMF and Ref. [28] for AMD.

Fragments are nearly isotropically distributed in space, in both models. This is shown in Fig. 9, where we display the ratio, R_Z, between the fragment yield observed in the angular domain $60 < \theta < 120$ (rescaled by a factor 2) and the total yield, as a function of the fragment charge. Apart from fluctuations of statistical origin, we notice a lack of small fragments in the selected angular domain in the SMF case,

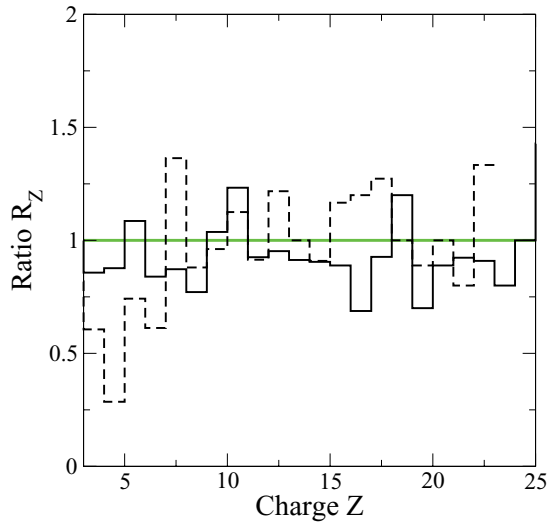

FIG. 9. (Color online) Ratio R_Z between the fragment yield observed in the angular domain $60 < \theta < 120$ (rescaled by a factor 2) and the total yield, as a function of the fragment charge, evaluated at $t = 300$ fm/c for the same system of Fig. 8. Notations are the same as in Fig. 8.

pointing to a slightly lower degree of stopping, compared to AMD, as also discussed in Ref. [24]. We would like to stress that, especially in the case of SMF calculations, the degree of stopping reached in the collision is crucial in determining the following reaction path. Indeed, if the reaction time becomes too short, spinodal instabilities would not have enough time to develop [2].

The larger total mass of the "liquid" phase obtained in AMD is also reflected in the IMF multiplicity, which is shown in Fig. 10. In fact, the multiplicity of IMFs with charge $Z > 2$ is larger in AMD. However, if one selects only sizable fragments, with charge $Z > 6$, closer multiplicities are obtained in the two models (dashed lines), but still higher (by about 1 unit) in the AMD case. This difference may be expected from the fact that the total number of nucleons contained in these IMFs in AMD is still larger by about 15 than in SMF (compare dot-dashed lines in Fig. 6).

As discussed earlier, the average kinetic energy of nucleons emitted at the pre-equilibrium stage of the reaction is nearly the same in the two codes. However, the larger amount of nucleons emitted in SMF causes a considerable reduction of the energy available for the remaining fragmenting system. As a consequence, the energy (kinetic + internal) stored into IMFs turns out to be larger in AMD. More precisely, the fragment intrinsic excitation energy is close in the two models and amounts to $\epsilon/A \approx 3 \pm 1$ MeV (corresponding to temperatures $T \approx 5$ MeV), whereas according also to the different compression-expansion dynamics (see Sec. III A), the fragments have higher collective velocities in AMD.

The fragment average kinetic energy is represented as a function of the fragment charge in Fig. 11. The dashed lines correspond to the time instant $t = 200$ fm/c, whereas solid lines are for fragments at $t = 600$ fm/c, where they have been accelerated by the Coulomb repulsion. One can notice that in the AMD case, these Coulomb acceleration effects are not so pronounced, because fragments are somewhat distant from each other already at $t = 200$ fm/c (see Fig. 4). The shape of the average kinetic energy, with an almost linear increase up to charges around $Z = 15$, denotes the presence of a collective flow velocity, as is also experimentally observed in similar reactions [42]. Fragments with larger size that probably emerge from the coalescence of two or more smaller objects and are more likely located closer to the system center of mass, are slowed down. The difference between the final average kinetic energy per nucleon in the two models amounts to 20%.

D. Isospin effects

It is very interesting to investigate also the isotopic content of pre-equilibrium and fragment emission, in connection with the asy-EOS employed and the details of the dynamical models

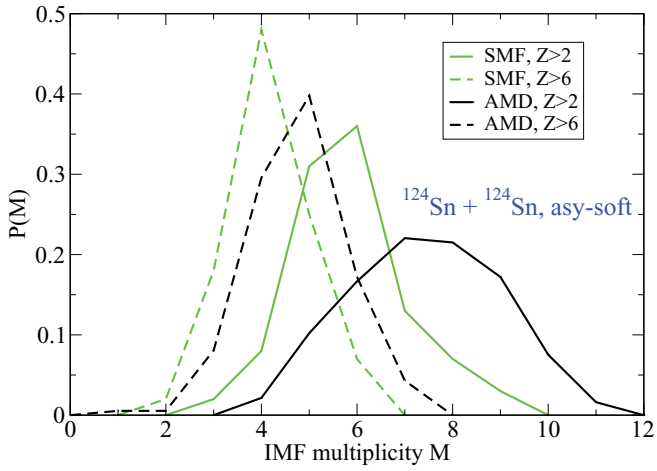

FIG. 10. (Color online) IMF multiplicity distribution as obtained in the two models for the same reaction of Fig. 8, at $t = 300$ fm/c. Solid lines, IMFs with charge $Z > 2$ are considered; dashed lines, IMFs with charge $Z > 6$ are considered.

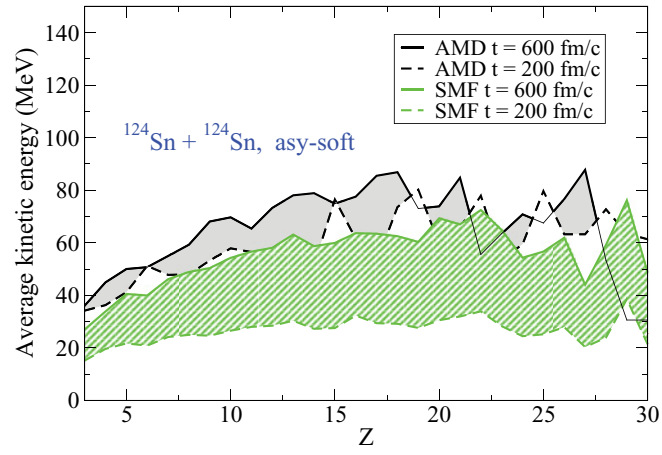

FIG. 11. (Color online) IMF average kinetic energy as a function of the charge Z, as obtained in the two models at $t = 200$ fm/c (dashed lines) and at $t = 600$ fm/c (solid lines), for the same reaction of Fig. 8. The solid and hatched gray areas mark the change during this time interval for AMD and SMF, respectively.

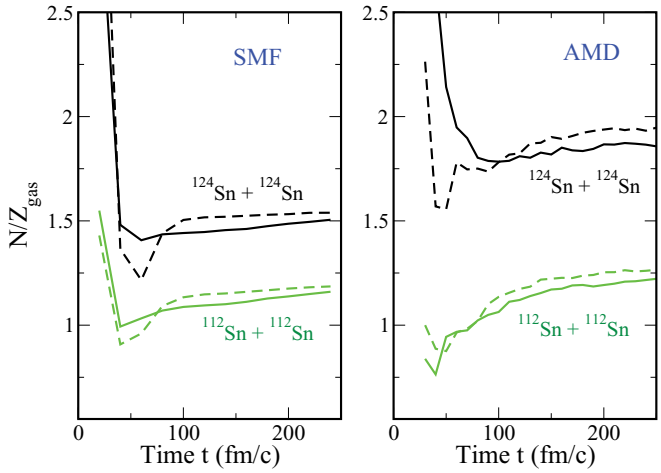

FIG. 12. (Color online) Time evolution of the N/Z content of the pre-equilibrium emission, as obtained in the two models (left and right panels), for the ^{112}Sn + ^{112}Sn and ^{124}Sn + ^{124}Sn reactions. Solid lines, asy-stiff interaction; dashed lines, asy-soft.

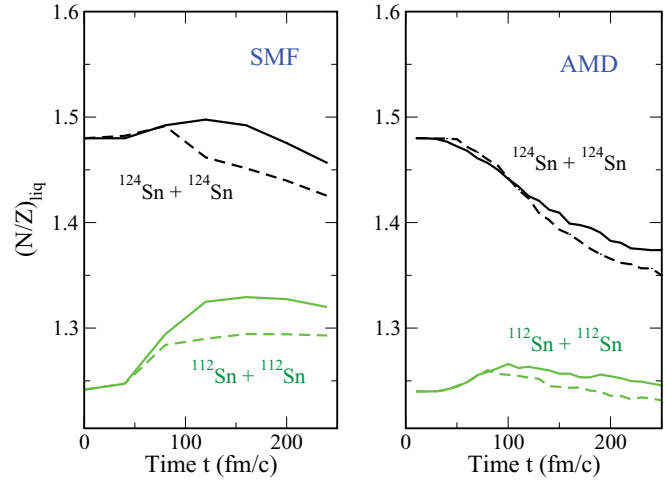

FIG. 13. (Color online) Time evolution of the isotopic content of the "liquid" phase, as obtained in the two models (left and right panels), for the ^{112}Sn + ^{112}Sn and ^{124}Sn + ^{124}Sn reactions. Solid lines, asy-stiff interaction; dashed lines, asy-soft.

under investigation. Differences between the two models are seen not only for the abundance of the pre-equilibrium emission, but also for its isotopic content. This is illustrated in Fig. 12, which shows the time evolution of the $(N/Z)_{\rm gas}$ ratio of emitted particles with $A \leqslant 4$, in both models, for the two iso-EOSs and the two reactions considered. The different calculations present some common features. In fact, we observe in all cases that the two curves of different asy-EOSs cross at times t around 70–100 fm/c, which is more evident for the neutron-rich system. According to the compression-expansion dynamics followed by the composite nuclear system, the crossing is connected to the fact that the system gradually evolves from a compact shape (compression, high density) where the symmetry energy is larger and the system likes to emit more neutrons in the asy-stiff case, to a dilute configuration (expansion, low density) where the symmetry energy is larger in the asy-soft case.

The results of Fig. 12 can be connected to the differences observed along the compression-expansion dynamics in the two models. In fact, as discussed in Sec. III A, within the SMF trajectory the composite nuclear system may enter lower density regions as a nearly homogeneous source and for a longer time, compared to the path followed in AMD. Hence the moderate $(N/Z)_{\rm gas}$ of the pre-equilibrium emission observed in SMF can be explained by the somewhat small value of the symmetry energy at lower density. This explanation is also consistent with the more abundant emission obtained in SMF calculations, because particles are less bound at low density. On the other hand, the $(N/Z)_{\rm gas}$ ratio in the AMD case is much larger, especially for the neutron-rich ^{124}Sn reaction. From the efficient clustering effects in AMD, protons are trapped in fragments that appear at early times, optimizing the symmetry energy of the whole system.

The same isospin effects can be also observed by looking at the isotopic content of fragments. Figure 13 shows the $(N/Z)_{\rm liq}$ content of the "liquid" phase (associated with the composite nuclear source at early times and with IMF's at later times), as obtained in the two models and with the two parametrizations of the symmetry energy. As expected already from the results concerning nucleon and light cluster emission, the "liquid" is more neutron rich in SMF. One can notice that, for the neutron-poor system in Fig. 13, the $(N/Z)_{\rm liq}$ ratio starts to increase at early times, which is from the repulsive effect of the Coulomb interaction and is related to the observation in Fig. 12 that $(N/Z)_{\rm gas}$ is smaller than the N/Z ratio of the total system. This increasing trend of $(N/Z)_{\rm liq}$ is more pronounced in the SMF model, because of the more abundant emission in this case. For the neutron-rich system, the initial increase of $(N/Z)_{\rm liq}$ is weak and observed only in the SMF case. The $(N/Z)_{\rm liq}$ ratio turns out to decrease approximately when fragments appear and neutrons are emitted, lowering the fragment symmetry energy (isospin distillation [34]). This effect is more pronounced in the soft case and happens at earlier times in AMD. Moreover, isospin distillation is stronger in the neutron-rich system.

At the end, one can see from Figs. 12 and 13 that the difference between the predictions of the two models is larger than the difference between the results associated with the two iso-parametrizations. This observation should be taken as a warning that the symmetry energy cannot be extracted from merely the N/Z content of the reaction products in a model-independent way.

IV. CONCLUSIONS

In this article we have undertaken a quantitative comparison of the features observed in heavy-ion fragmentation reactions at Fermi energies, as predicted by two transport models: SMF and AMD. As far as observables of experimental interest are concerned, one significant discrepancy between the two models is connected to the amount of pre-equilibrium emission (i.e., the energetic particles that leave the system at the early stage of the reaction). In AMD, clustering effects appear to be more relevant, reducing the amount of free

nucleons emitted, compared to SMF, in favor of a richer production of primary light IMFs. The yield of sizable primary IMFs ($Z > 6$) is close in the two models. However in SMF fragments with charge around 10 are slightly more abundant, whereas in AMD the tail at larger Z (around 20) is more pronounced. The shape of the SMF charge distribution is closer to the expectations of spinodal decomposition [2]. However, it should be noticed that these differences can be smoothened by secondary decay effects [41]. In fact, both models are able to fit (final) experimental charge distributions (of IMFs) reasonably well [28,43]. In SMF, fragment kinetic energies are smaller, compared to AMD, by about 20%. These observations corroborate the scenario of a faster fragmentation process in AMD, whereas in SMF the system spends a longer time as a nearly homogeneous source at low density, emitting a larger amount of nucleons prior to fragment formation.

Another interesting feature is that the N/Z ratio of the pre-equilibrium emission and of primary IMFs is different in the two models. For a fixed parametrization of the symmetry potential, the isotopic content of the emitted particles is systematically lower in SMF, where the emission is more abundant. As a consequence, IMFs are more neutron rich in SMF than in AMD. The latter observation leads to the conclusion that isotopic properties are largely affected by the reaction dynamics. This can be expected just from the fact that the symmetry energy is density dependent, so isospin observables should keep the fingerprints of the density regions spanned in the collision. However, the impact of the reaction path on these observables may be more intricate. From this point of view, isospin properties can be also considered as a good tracer of the reaction mechanism and may contribute to probe the corresponding fragmentation path. Hence, the discrepancy between the two models may be ascribed essentially to the different compression-expansion dynamics and clusterization effects that, as shown by our results, affect isoscalar as well as isovector properties of the reaction products.

Therefore, the simultaneous analysis of several experimental observables in nuclear reactions at Fermi energies should help to shed light on the underlying fragmentation mechanism and the corresponding role of mean-field and many-body correlations. In other words, a check of the global reaction dynamics could be a way to test the validity of the approximations employed in the dynamical models devised to deal with the complex many-body problem. One may look at suitable isoscalar observables such as fragment and particle yields and energy spectra, as well as at the isotopic content of the reaction products. As shown in Fig. 6, the sharing between the yields of light IMFs and light particles ($A \leqslant 4$) is somewhat different in the two models, the latter being more abundant and less neutron rich in SMF. In particular, the study of pre-equilibrium emission, which is not influenced by secondary decay effects, could really help to probe the reaction dynamics, because the difference between AMD and SMF predictions is somewhat large; see the results of Figs. 6, 7, and 12. Only when the model reliability is established, can one undertake a deeper investigation of isospin observables, from which more detailed information on the symmetry energy and its density dependence can be accessed. Indeed, as shown in Figs. 12 and 13, the differences between predictions corresponding to two commonly employed symmetry energy parametrizations are smaller than the differences associated with the two models considered here.

Finally, it would be appealing to extend our comparison of multifragmentation reactions to other approaches introduced to follow the many-body dynamics [15,18,20]. In such a context, new developments of stochastic mean-field models, in the direction of introducing fluctuations in full phase space [23] and enhancing the role of correlations, are also of interest.

ACKNOWLEDGMENTS

We thank M. Di Toro for useful comments and discussions. We also acknowledge the European Center for Theoretical Studies in Nuclear Physics and Related Areas (ECT*, Trento, Italy) for inspiring discussions during workshops on numerical simulations of heavy-ion reactions. This work is supported by Grant-in-Aid for Scientific Research (KAKENHI) Grant No. 21540253 from Japan Society for the Promotion of Science, and partly by High Energy Accelerator Research Organization (KEK) as a supercomputer project.

[1] B. Borderie and M. F. Rivet, Prog. Part. Nucl. Phys. **61**, 551 (2008).
[2] Ph. Chomaz, M. Colonna, and J. Randrup, Phys. Rep. **389**, 263 (2004).
[3] D. R. Bowman *et al.*, Phys. Rev. Lett. **67**, 1527 (1991).
[4] G. Bertsch and P. J. Siemens, Phys. Lett. B **126**, 9 (1983).
[5] Ph. Chomaz and F. Gulminelli, Nucl. Phys. A **647**, 153 (1999).
[6] P. Chomaz and F. Gulminelli, Eur. Phys. J. A **30**, 317 (2006).
[7] J. B. Elliott *et al.*, Phys. Rev. Lett. **88**, 042701 (2002).
[8] M. D'Agostino *et al.*, Nucl. Phys. A **699**, 795 (2002).
[9] G. Tabacaru *et al.*, Eur. Phys. J. A **18**, 103 (2003).
[10] H. S. Xu *et al.*, Phys. Rev. Lett. **85**, 716 (2000).
[11] E. Geraci *et al.*, Nucl. Phys. A **732**, 173 (2004).
[12] T. Furuta and A. Ono, Phys. Rev. C **79**, 014608 (2009).
[13] A. H. Raduta, M. Colonna, V. Baran, and M. Di Toro, Phys. Rev. C **74**, 034604 (2006); A. H. Raduta, M. Colonna, and M. Di Toro, *ibid.* **76**, 024602 (2007).
[14] A. Ono, Phys. Rev. C **59**, 853 (1999).
[15] J. Aichelin, Phys. Rep. **202**, 233 (1991).
[16] H. Feldmeier, Nucl. Phys. A **515**, 147 (1990).
[17] A. Ono, H. Horiuchi, T. Maruyama, and A. Ohnishi, Phys. Rev. Lett. **68**, 2898 (1992); Prog. Theor. Phys. **87**, 1185 (1992).
[18] M. Papa, T. Maruyama, and A. Bonasera, Phys. Rev. C **64**, 024612 (2001).
[19] M. Colonna and Ph. Chomaz, Phys. Lett. B **436**, 1 (1998).
[20] N. Wang, Z. X. Li, X. Z. Wu, J. Tian, Y. X. Zhang, and M. Liu, Phys. Rev. C **69**, 034608 (2004).
[21] S. Ayik and C. Gregoire, Phys. Lett. B **212**, 269 (1988).

[22] J. Randrup and B. Remaud, Nucl. Phys. A **514**, 339 (1990).
[23] J. Rizzo, P. Chomaz, and M. Colonna, Nucl. Phys. A **806**, 40 (2008).
[24] J. Rizzo, M. Colonna, and A. Ono, Phys. Rev. C **76**, 024611 (2007).
[25] J. Rizzo, M. Colonna, M. Di Toro, and V. Greco, Nucl. Phys. A **732**, 202 (2004).
[26] A. Guarnera, M. Colonna, and Ph. Chomaz, Phys. Lett. B **373**, 267 (1996).
[27] M. Colonna *et al.*, Nucl. Phys. A **642**, 449 (1998).
[28] A. Ono, S. Hudan, A. Chbihi, and J. D. Frankland, Phys. Rev. C **66**, 014603 (2002).
[29] A. Ono and H. Horiuchi, Prog. Part. Nucl. Phys. **53**, 501 (2004).
[30] C. Gale, G. M. Welke, M. Prakash, S. J. Lee, and S. Das Gupta, Phys. Rev. C **41**, 1545 (1990).
[31] V. Greco, Ph.D. thesis, University of Catania (Italy), 1997; V. Greco, A. Guarnera, M. Colonna, and M. Di Toro, Phys. Rev. C **59**, 810 (1999); Nuovo Cimento A **111**, 865 (1998).
[32] *Isospin Physics in Heavy Ion Collisions at Intermediate Energies*, edited by B.-A. Li and W. Udo Schröder (Nova Science Publishers, New York, 2001).
[33] I. Bombaci, "EOS for isospin-asymmetric nuclear matter for astrophysical applications," in Ref. [32] pp. 35–81 and references therein.
[34] V. Baran, M. Colonna, V. Greco, and M. Di Toro, Phys. Rep. **410**, 335 (2005).
[35] M. Colonna and M. B. Tsang, Eur. Phys. J. A **30**, 165 (2006).
[36] V. Baran *et al.*, Nucl. Phys. A **703**, 603 (2002).
[37] J. Dechargé and D. Gogny, Phys. Rev. C **21**, 1568 (1980).
[38] A. Ono, P. Danielewicz, W. A. Friedman, W. G. Lynch, and M. B. Tsang, Phys. Rev. C **68**, 051601(R) (2003).
[39] G. Batko and J. Randrup, Nucl. Phys. A **563**, 97 (1993).
[40] C. O. Dorso and J. Randrup, Phys. Lett. B **301**, 328 (1993).
[41] M. Colonna *et al.*, Nucl. Phys. A **742**, 337 (2004).
[42] N. Marie *et al.*, Phys. Lett. B **391**, 15 (1997).
[43] J. D. Frankland *et al.*, Nucl. Phys. A **689**, 940 (2001).